Chapter 7

Topological Hall effect

7.1 Introduction

During the last decades, a wide range of Hall effects has appeared in the literature [25, 27, 33]. In the classical Hall effect, discovered more than a century ago, the Lorentz force resulting from a magnetic field B_z applied perpendicular to a two-dimensional sample gives rise to an electric field E_y perpendicular to the applied current I_x through the sample. As a result, a transverse resistivity $\rho_{xy} = E_y/j_x$ can be defined (j_x is the current density). The Drude model [87] shows that this resistivity is linear in the magnetic field[1]: $\rho_{xy} = R_0 B_z$, with the Hall coefficient $R_0 = \frac{1}{n_q q}$ (q is the charge of the current carriers, n_q the carrier density).

In ferromagnetic systems, an extra contribution to the off-diagonal resistivity was found: $\rho_{xy} = R_0 B_z + R_s M$. This anomalous contribution is proportional to the magnetization M, and gives rise to a Hall effect even in the absence of an externally applied magnetic field. A lot of experimental work was devoted to this so-called anomalous Hall effect, and resulted in some empirical laws for the coefficient R_s. Nevertheless, it took more than sixty years to clear up the origin of the effect theoretically. Finally, it was agreed upon that the effect is due to spin-orbit coupling, which gives rise to two scattering mechanisms, skew scattering [88–90] and side jump [91, 92], that introduce different preferential scattering directions for spin-up and spin-down particles. As a result, the incoming spin-up particles would be scattered towards one edge of the sample, and spin downs to the opposite edge. In a ferromagnet, the spin subbands are unequally populated and this spin scattering imbalance leads to a charge accumulation at opposite edges, creating a transverse electrical field and thus explaining the anomalous contribution to the off-diagonal resistivity[2].

---

[1] In high magnetic fields, the linear relation between ρ_{xy} and B_z breaks down: instead ρ_{xy} shows flat plateaus with quantized resistance values at $\rho_{xy} = h/(n2e^2)$ with n integer. This is called the quantum Hall effect, and was discovered experimentally in the beginning of the eighties [33].

[2] In a normal semiconductor, the same spin-orbit scattering mechanisms are present, and although in this case there is no net charge accumulation, there will be a spin accumulation at opposite edges, giving rise to the so-called spin Hall effect [25].

Very recently however, the behavior of the anomalous coefficient R_s in certain types of frustrated ferromagnetic systems with noncoplanar magnetic moments, like some pyrochlore-type compounds [93] or spin glasses [94], was found to be in contradiction with the expectations from the spin-orbit scattering theory. In order to explain the anomalous Hall effect in these systems, a mechanism was proposed based on the Berry phase [95] an electron acquires when its spin follows the spatially varying magnetization that is present in such materials [96]. Since the effect can be attributed to the topology of the magnetization texture, the term topological Hall effect was coined [32].

However, a quantitative comparison between the proposed theory and the experiments on, e.g., the pyrochlore compounds proves to be difficult: in experiments, both the spin-orbit scattering and the Berry phase mechanism are simultaneously present, and it is therefore difficult to distinguish between them. Making such a distinction is further complicated by the fact that quantitative experimental information on the magnetization texture is not easily available as the magnetization varies on the microscopic scale in the considered compounds. In Ref. [32], it was therefore proposed to study the topological Hall effect in a two-dimensional electron gas (2DEG). In such a system an artificial magnetization texture can be introduced by the stray field of a lattice of ferromagnetic nanocylinders placed above the 2DEG. The advantage of such a setup is that all relevant parameters of the texture can be controlled to some extent by changing the nanocylinder lattice geometry, and that one can concentrate purely on the topological effect since spin-orbit scattering effects can be made small by choosing a semiconductor material with a small spin-orbit coupling constant for creating the 2DEG.

Theoretical studies of the topological Hall effect have mainly concentrated on the adiabatic regime, where the electron spin aligns perfectly with the local magnetization during its movement [32, 96, 97]. On the other hand, only very few papers have dealt with the nonadiabatic limit [98, 99], and even less is known about the transition between the two regimes. In this chapter therefore, we will study the topological Hall effect in the 2DEG systems mentioned above and we will try to improve our understanding of the effect in different regimes by means of numerical investigations.

The chapter is subdivided as follows. A short introduction to the Berry phase will be given first. This will aid in understanding the mechanism behind the topological Hall effect. Next, the topological Hall effect will be studied numerically in the adiabatic regime, making use of some simple models for the magnetization texture. Subsequently, a short discussion about adiabaticity criteria follows, in which a long-standing question about the relevant criterion in the diffusive transport regime is pointed out. An answer to this question will be formulated on the basis of numerical results dealing with the transition point between the nonadiabatic and adiabatic regime for different values of the mean free path in the sample.

7.2 Berry phase

7.2.1 Generalities

Although geometric phases in quantum physics are quite a young topic, a few textbooks have already appeared in which the origin and the mathematical description of such phases, together with their applications, have been discussed in detail [100, 101]. This proves the current high interest in the subject. In this section, only a brief account will be given on the Berry phase, discussing the main principles that are relevant for understanding the topological Hall effect in the next section. Parts of the discussion will proceed along the lines of what can be found in Refs. [95, 102–104].

We will start from a general "vector object" that is transported along a closed path on a curved surface, as depicted in Fig. 7.1. Even if the vector is not allowed to rotate around the normal to the surface at each point it passes (parallel transport), it will have been rotated over an angle Ω when returning to the starting position. The vector thus does not return to its initial state. This effect is of a purely geometrical/topological origin and is related to the intrinsic curvature of the surface on which the vector is transported. When moving the vector in a plane, or on the surface of a cylinder, no such phenomenon will occur.

In principle, quantum states are also described by vectors in a more abstract state space. Therefore they can "rotate" in a similar way when they are transported. The transport we have in mind now is not necessarily related to a physical motion. Rather, we are interested in how a particular eigenstate $|n[\mathbf{R}]\rangle$ evolves under influence of a Hamiltonian $H[\mathbf{R}]$ when some external parameters $\mathbf{R} = (R_1, R_2, \ldots)$ on which the Hamiltonian depends change in time: $\mathbf{R} = \mathbf{R}(t)$. In particular, we will ask how the final state $|n[\mathbf{R}(T)]\rangle$ differs from the initial state $|n[\mathbf{R}(0)]\rangle$ when the parameters in the Hamiltonian are carried adiabatically around some closed path $\mathcal{C} = \{\mathbf{R}(t)|t = 0 \rightarrow T, \mathbf{R}(T) = \mathbf{R}(0)\}$ in parameter space. To answer this question, one can proceed as follows.
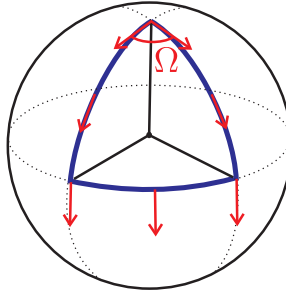

Figure 7.1: Parallel transport of a vector along a closed path on a sphere. When the vector arrives back at its starting position, it has undergone a rotation over an angle Ω.

For every set $\mathbf{R}$ of parameters, we can find the eigenstates $|n[\mathbf{R}]\,\rangle$ and their corresponding eigenvalues $E_n[\mathbf{R}]$ from the time-independent Schrödinger equation

$$H[\mathbf{R}]|n[\mathbf{R}]\,\rangle = E_n[\mathbf{R}]|n[\mathbf{R}]\,\rangle. \tag{7.1}$$

A first important point to note here is that this equation only defines the eigenvectors $|n[\mathbf{R}]\,\rangle$ up to a phase factor. We will assume that a particular choice of this phase has been made, only requiring that the ket $|n[\mathbf{R}]\,\rangle$ changes smoothly within the parameter range of interest, and that it is single valued for every $\mathbf{R}$.

Now suppose that the system initially starts in an eigenstate $|\psi(t=0)\,\rangle = |n[\mathbf{R}(t=0)]\,\rangle$. When the external parameters $\mathbf{R}(t)$ change sufficiently slow compared to typical orbital frequencies $\Delta E_n(t)$, the adiabatic theorem [105] states that the system will remain in the eigenstate $|n[\mathbf{R}(t)]\,\rangle$, picking up at most a time-dependent phase factor[3]. As such, we can write

$$
\begin{aligned}
|\psi(t)\,\rangle &= e^{\mathrm{i}\alpha(t)}\,|n[\mathbf{R}(t)]\,\rangle \\
&= e^{-\frac{\mathrm{i}}{\hbar}\int_0^t \mathrm{d}t'\, E_n(t')}\, e^{\mathrm{i}\gamma_n(t)}\,|n[\mathbf{R}(t)]\,\rangle,
\end{aligned}
\tag{7.2}
$$

where in the second equation we have splitted off the usual dynamical phase factor which is a generalization of the phase picked up during the time evolution of an eigenstate evolving under a time-independent Hamiltonian. Inserting this in the Schrödinger equation (7.1), one finds for the phase $\gamma_n(t)$:

$$
\begin{aligned}
\frac{\mathrm{d}\gamma_n}{\mathrm{d}t}(t) &= \mathrm{i}\langle\, n[\mathbf{R}(t)]\,|\,\mathrm{d}n[\mathbf{R}(t)]/\mathrm{d}t\,\rangle \tag{7.3a} \\
&= \mathrm{i}\langle\, n[\mathbf{R}(t)]\,|\,\nabla_{\mathbf{R}} n[\mathbf{R}(t)]\,\rangle \cdot \frac{\mathrm{d}\mathbf{R}}{\mathrm{d}t}(t). \tag{7.3b}
\end{aligned}
$$

All this, namely that the dynamical phase is accompanied by a phase $\gamma_n(t)$ that satisfies Eq. (7.3) was already known since the development of the adiabatic theorem, and there is thus nothing new about it. However, it was always assumed that a gauge transformation can be undertaken so as to redefine the phase of the basis vectors $|n[\mathbf{R}]\,\rangle$ (remember that this phase was not uniquely defined) in such a way that the phase factor $\gamma_n(t)$ would be eliminated. If this would be possible, this phase does not have any physical meaning as it would be gauge dependent.

It was Berry who realized that such a gauge transformation cannot be defined globally because $\gamma_n(t)$ will depend on the geometry of the path taken in parameter space, and $\gamma_n(t)$ at a certain time t will therefore be different for different paths [95]. Thus γ_n cannot be written as a function of $\mathbf{R}$ alone, and a gauge transformation of the form $|n[\mathbf{R}]\,\rangle \rightarrow e^{\mathrm{i}\gamma_n(\mathbf{R})}|n[\mathbf{R}]\,\rangle$ cannot be defined uniquely. In particular $\gamma_n(t)$ is not single valued under continuation around a circuit: if $\mathbf{R}$ evolves along a closed path so that $\mathbf{R}(T) = \mathbf{R}(0)$, then $\gamma_n(T)$ is not equal to $\gamma_n(0)$ and the difference will depend on the geometrical details of the path taken. The phase

---

[3]At least when $|n[\mathbf{R}]\,\rangle$ is nondegenerate for all $\mathbf{R}$, which we will assume here.

$\gamma_n(T)$ could thus in principle easily be observed by setting up an interference experiment between the states $|n[\mathbf{R}(t=0)]\rangle$ and $|n[\mathbf{R}(t=T)]\rangle$.

A possible "gedanken experiment" illustrating the statements above is the following [95]. A mono-energetic beam of electrons polarized along a magnetic field $\mathbf{B}$ is split at some point in two separate beams. One beam moves along a path where the magnetic field is kept constant, while the other beam will experience a field $\mathbf{B}(t)$ that slowly rotates around a cone. When the rotating field has returned to its original direction, the two beams are recombined to interfere. If the spin follows adiabatically the field direction, then according to the theory above, the second beam will pick up an extra phase γ_n compared to the first one. This phase difference γ_n can be modified by altering the geometry of the path that is followed by the magnetic field: in this example this could be realized by changing the angle θ of the cone. Doing so, the interference between both beams can be modulated between constructive and destructive, and the geometrical phase could in principle be visualized.

So it is the phase that is picked up when the external parameters describe a closed path that can be attributed a clear physical meaning and is called the Berry phase. This phase can be written as

$$
\begin{align}
\gamma_n(T) - \gamma_n(0) = \gamma_n(\mathcal{C}) \;&=\; \int_0^T \mathrm{d}t\, \frac{\mathrm{d}\gamma_n}{\mathrm{d}t}(t) \tag{7.4a}\\[6pt]
&=\; \mathrm{i}\int_0^T \mathrm{d}t\, \frac{\mathrm{d}\mathbf{R}}{\mathrm{d}t} \cdot \langle\, n[\mathbf{R}(t)]\,|\,\nabla_{\mathbf{R}} n[\mathbf{R}(t)]\,\rangle \tag{7.4b}\\[6pt]
&=\; \mathrm{i}\oint \mathrm{d}\mathbf{R} \cdot \langle\, n[\mathbf{R}(t)]\,|\,\nabla_{\mathbf{R}} n[\mathbf{R}(t)]\,\rangle \tag{7.4c}
\end{align}
$$

where the last integration is along the closed loop in parameter space. The physical significance of this phase can be made more clear by writing $\gamma_n(\mathcal{C})$ as

$$
\begin{align}
\gamma_n(\mathcal{C}) \;&=\; \mathrm{i}\oint \mathrm{d}\mathbf{R} \cdot \mathbf{A}_n(\mathbf{R}) \tag{7.5}\\[6pt]
&=\; \iint_{S_{\mathcal{C}}} \mathrm{d}S\;\nabla\times\mathbf{A}_n(\mathbf{R}), \tag{7.6}
\end{align}
$$

with the "vector potential"

$$
\mathbf{A}_n(\mathbf{R}) = \mathrm{i}\langle\, n[\mathbf{R}]\,|\,\nabla_{\mathbf{R}} n[\mathbf{R}]\,\rangle. \tag{7.7}
$$

In Eq. (7.6), Stokes theorem[4] has been used to write the path integral in terms of an integral over the surface $S_{\mathcal{C}}$ bounded by the path $\mathcal{C}$. Although the vector potential $\mathbf{A}_n(\mathbf{R})$ is not gauge invariant and therefore not an observable quantity, the Berry phase is. Indeed, consider a general gauge transformation $|n\rangle \to e^{\mathrm{i}\xi(\mathbf{R})}|n\rangle$

---

[4]Stokes theorem should be suitably generalized when the vector $\mathbf{R}$ is not three-dimensional. This is possible using the language of differential geometry [101].

changing the phases of the basis vectors. This will change $\mathbf{A}_n \rightarrow \mathbf{A}_n + i\nabla\xi$, but since $\nabla \times \nabla\xi = 0$, the Berry phase $\gamma_n(\mathcal{C})$ stays invariant under such a transformation.

Looking back at Eqs. (7.4), the Berry phase depends only on the geometry of the closed path $\mathcal{C}$ that is traversed by $\mathbf{R}(t)$ in parameter space. It is therefore called a geometrical phase. On the other hand, the dynamical phase [see Eq. (7.2)] is dependent upon the rate at which the path in parameter space is completed, and thus gives us information about the time evolution of the system. Roughly speaking, the dynamical phase results from a local rotation of the state vector, while the Berry phase is analogous to a rotation due to parallel transport.

Several restrictions on the states $|n[\mathbf{R}]\rangle$ were made in deriving the Berry phase. Since the original paper by Berry, most of them have been loosened: e.g., degenerate basis states were treated in Ref. [106], while in Ref. [107] it was shown that even during a nonadiabatic evolution a geometrical phase will be picked up.

7.2.2 A simple example

The classic example illustrating Berry's phase is that of an electron at the origin subjected to a magnetic field $\mathbf{B}(t)$ of constant magnitude but changing direction, as depicted in Fig. 7.2.
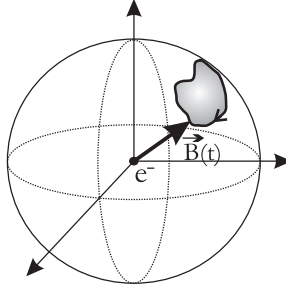

Figure 7.2: Electron in a time-dependent magnetic field. When the field describes a closed trajectory along the surface of a sphere, the electron will pick up a Berry phase.

The Hamiltonian for this problem is given by

$$H = -g\,\mathbf{B}(t)\cdot\boldsymbol{\sigma}, \qquad (7.8)$$

with $\boldsymbol{\sigma}$ the vector of Pauli spin matrices, and g a coupling constant. In this case, the external parameters $\mathbf{R}(t)$ on which the Hamiltonian depends are the spherical angles describing the direction of the time-dependent field: $\mathbf{R}(t) = [\theta(t), \phi(t)]$.

The electron spin will follow the field direction adiabatically whenever

$$\omega_s/\omega \gg 1, \qquad (7.9)$$

where $\omega_s = eB/m^*$ is the spin precession frequency, and ω is the rotation fre-

quency of the magnetic field $\mathbf{B}(t)$[5]. The state of the electron is then given by the spin-up spinor with respect to $\mathbf{B}(t)$:

$$|n_+[\theta, \phi]\rangle = \begin{pmatrix} \cos\frac{\theta}{2}\, e^{-\mathrm{i}\phi} \\ \sin\frac{\theta}{2} \end{pmatrix}. \tag{7.10}$$

To calculate the Berry phase picked up when the magnetic field follows a closed path, we need the quantity $\nabla \times \langle n_+|\nabla n_+\rangle$. Expressing the gradient operator in spherical coordinates, we find

$$\nabla \times \langle n_+|\nabla n_+\rangle = \frac{\mathrm{i}}{2r^2}\mathbf{e}_r, \tag{7.11}$$

where r is the radial component of the magnetic field, and $\mathbf{e}_r$ is a unit vector in this direction. Using Eq. (7.4c), one finds for the Berry phase

$$\gamma_+(\mathcal{C}) = -\frac{1}{2}\int \frac{1}{r^2}\,\mathbf{e}_r \cdot \mathrm{d}\mathbf{S}. \tag{7.12}$$

The integral is over the area on the sphere swept out by $\mathbf{B}$ in the course of its closed path, so $\mathrm{d}\mathbf{S} = r^2 \mathrm{d}\Omega\,\mathbf{e}_r$, and hence

$$\gamma_+(\mathcal{C}) = -\frac{1}{2}\int \mathrm{d}\Omega = -\frac{1}{2}\Omega. \tag{7.13}$$

So the net geometric phase picked up by the electron will be half of the solid angle Ω subtended by the path the magnetic field followed on the sphere. In the derivation, it was implicitly assumed that the magnetic field rotates clockwise. For a counterclockwise rotation, the Berry phase will just change its sign. The obtained result is very simple, but the physics behind it will in principle suffice for understanding the physical origin of the topological Hall effect.

7.3 Topological Hall effect

7.3.1 Theory

When an electron moves in a two-dimensional electron gas which is subjected to a spatially varying magnetization, it will follow the local magnetization direction adiabatically when the magnetization is strong enough. In its rest frame, the electron will thus see a time-dependent magnetic field and, as explained in the simple example above, will pick up a Berry phase that depends on the solid angle subtended by the magnetization direction as the electron follows its path. As we will see next, the effect of this Berry phase can be mapped onto that of an effective magnetic flux applied perpendicular to the sample. By means of this mapping, it is clear then that the spatially varying magnetization and its related Berry phase can induce a Hall

---

[5]A derivation of this expression can be found in any textbook of quantum mechanics, e.g., in Ref. [105].

effect, which was termed topological Hall effect [32] as it depends solely on the topology of the magnetization texture in the sample and does not rely explicitly on spin-orbit coupling nor on any real magnetic flux piercing through the sample.

We will consider the following Hamiltonian:

$$H = -\frac{\hbar^2}{2m^*}\nabla^2 - g\,\mathbf{M}(\mathbf{r}) \cdot \boldsymbol{\sigma}. \tag{7.14}$$

The first term describes the kinetic energy of the electron in the 2DEG (m^* is its effective mass), while the second is the exchange splitting induced by a spatially varying magnetization $\mathbf{M}(\mathbf{r})$. We will assume the magnitude M of the magnetization to be constant, while its direction is position dependent: $\mathbf{M}(\mathbf{r}) = M\mathbf{n}(\mathbf{r})$, with $\mathbf{n}(\mathbf{r})$ a unit vector in the magnetization direction. For our numerical purposes, we need the tight-binding equivalent of this Hamiltonian (see Chap. 3):

$$\mathcal{H} = -t\sum_{\langle ij \rangle}\sum_{\alpha} |i\alpha\rangle\langle j\alpha| - gM\sum_{i}\sum_{\alpha,\beta} |i\alpha\rangle\,\boldsymbol{\sigma}_{\alpha\beta}\cdot\mathbf{n}_i\,\langle i\beta|, \tag{7.15}$$

where i, j label the lattice sites, α, β are spin indices, t is the hopping amplitude between neighboring sites, and $\mathbf{n}_i = \mathbf{n}(\mathbf{r}_i)$. We can define a basis set $\{|i, \pm\rangle\}$ of states at site i with their spin parallel (+) or antiparallel (-) with respect to the magnetization direction at that site:

$$|i, +\rangle = \begin{pmatrix} \cos\frac{\theta_i}{2}\,e^{-\mathrm{i}\phi_i} \\ \sin\frac{\theta_i}{2} \end{pmatrix}; \quad |i, -\rangle = \begin{pmatrix} -\sin\frac{\theta_i}{2} \\ \cos\frac{\theta_i}{2}\,e^{\mathrm{i}\phi_i} \end{pmatrix}, \tag{7.16}$$

where (θ_i, ϕ_i) are the spherical angles of the local magnetization direction $\mathbf{n}_i$. Defining the operators

$$\mathcal{P}_{\pm} = \sum_{i} |i, \pm\rangle\langle i, \pm|, \tag{7.17}$$

which project on the subspace spanned by the spin-up (-down) states, and using $\mathcal{P}_+ + \mathcal{P}_- = 1$, one can write

$$\mathcal{H} = \left(\mathcal{P}_+ + \mathcal{P}_-\right)\mathcal{H}\left(\mathcal{P}_+ + \mathcal{P}_-\right) \tag{7.18}$$

$$= \mathcal{P}_+\mathcal{H}\mathcal{P}_+ + \mathcal{P}_-\mathcal{H}\mathcal{P}_+ + \mathcal{P}_+\mathcal{H}\mathcal{P}_- + \mathcal{P}_-\mathcal{H}\mathcal{P}_-. \tag{7.19}$$

When the exchange splitting $\Delta = 2gM$ is large enough, the spin-up state with respect to the local magnetization direction will be energetically so favorable that spin-flip transitions will be absent. In this adiabatic regime, the electron spin will thus follow exactly the local magnetization direction as the electron moves through the 2DEG, so that we can confine ourselves to the subspace spanned by spin-up states and neglect all other terms in Eq. (7.19). Doing so, one finds an effective Hamiltonian governing the dynamics in the perfectly adiabatic regime [96, 108] (see Appendix F for a detailed derivation):

$$\mathcal{H}^{\mathrm{eff}} = \mathcal{P}_+\mathcal{H}\mathcal{P}_+ = -\sum_{\langle i,j \rangle} t_{ij}^{\mathrm{eff}}|i, +\rangle\langle j, +| - gM, \tag{7.20}$$
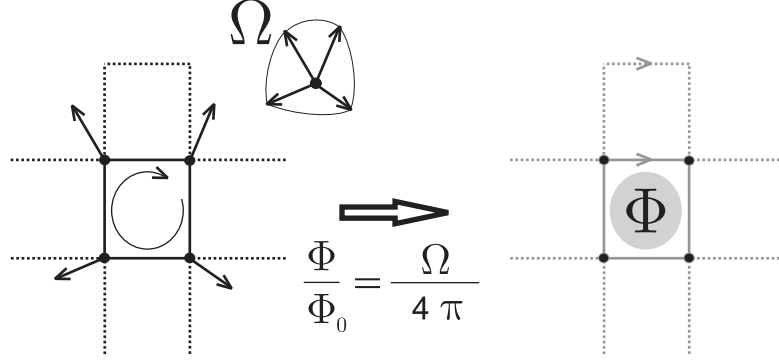
Figure 7.3: Mapping of an electron moving in a magnetic texture to a spinless electron moving around a flux tube distribution. The gray color of the vertices on the right picture stand for a change in hopping amplitude, while the arrows denote a change in hopping phase at the respective vertices.

with

$$t_{ij}^{\text{eff}} = t \cos\frac{\theta_{ij}}{2} e^{i\gamma_{ij}}. \tag{7.21}$$

As such, we have mapped the original problem to a free electron like tight-binding Hamiltonian, with renormalized hopping parameters between nearest neighbors. The magnitude of the hopping parameter is decreased depending on the angle θ_{ij} between the magnetization direction at sites i and j. But more importantly for us, a phase factor $e^{i\gamma_{ij}}$ is picked up, which describes the effect of the Berry phase. Let's see how this can be understood.

Suppose an electron makes a closed trajectory around a lattice cell as depicted in Fig. 7.3. Since its spin follows adiabatically the local magnetization direction, the electron will pick up a Berry phase that is equal to half the solid angle Ω subtended by the magnetization directions at the four corners of the cell. On the other hand, when a magnetic flux $\Phi = Ba^2$ would pierce through the same lattice cell, an electron moving around it would acquire a phase $2\pi\Phi/\Phi_0$ ($\Phi_0 = h/e$ is the magnetic flux quantum). So in principle, the effect of the Berry phase picked up around a lattice cell is equivalent to that of a magnetic flux $\Phi/\Phi_0 = \Omega/4\pi$ piercing through this cell.

This analogy becomes more clear when looking back at the Peierls method we used for describing such a flux tube: the hopping parameters in the complete lattice were changed as

$$t_{ij} \rightarrow t\, e^{-ie/\hbar \int_i^j \mathbf{A} \cdot d\mathbf{l}}, \tag{7.22}$$

in which $\mathbf{A}$ describes the vector potential generated by the flux tube. Comparing with Eq. (7.21), we see that the γ_{ij} can be generated by the same vector potential $\mathbf{A}$ describing flux tubes with values of $\Phi/\Phi_0 = \Omega/(4\pi)$ piercing through the lattice

cells:

$$\gamma_{ij} = -e/\hbar \int_i^j \mathbf{A} \cdot \mathrm{d}\mathbf{l}. \tag{7.23}$$

So for expressing the γ_{ij}, one can proceed as follows. One calculates the solid angle subtended by the magnetization directions at the corners of every single lattice cell, and translates this into a flux tube distribution with fluxes $\Phi/\Phi_0 = \Omega/(4\pi)$. Subsequently, one describes this flux tube arrangement in terms of a vector potential $\mathbf{A}$, and calculates the phases γ_{ij} with Eq. (7.23). As such, the γ_{ij} are uniquely defined once we have made a choice of gauge for the vector potential $\mathbf{A}$ describing the flux tubes. For example, for describing the effect of a single flux tube, one could make a choice of gauge for $\mathbf{A}$ such that the hopping phase on all the vertices above the flux tube change as $t \rightarrow t \exp(\mathrm{i}2\pi\Phi/\Phi_0) = t \exp(\mathrm{i}\Omega/2)$ (see Fig. 7.3). This would correspond to the same gauge we used in Sec. 3.1.2 for describing inhomogeneous magnetic fields.

In summary, the Hamiltonian for an electron moving in a magnetization texture can be mapped onto a Hamiltonian of spinless electrons moving in an inhomogeneous magnetic flux distribution. The former will be referred to as the magnetization model, while the latter will be called the flux model. In the flux model, the value of the effective magnetic flux through a lattice cell is given by $\Phi/\Phi_0 = \frac{\Omega}{4\pi}$, where Ω is the solid angle subtended by the magnetization directions at the four corners of the lattice cell. Also, the magnitude of the hopping parameters depends on the angle between the magnetization directions. By means of this mapping it should be clear now that the magnetization texture can indeed give rise to a Hall effect. Since the effective flux is given by a solid angle, it is obvious that the topological Hall effect can be nonzero only for noncoplanar textures.

7.3.2 A first example

The existence of the topological Hall effect will now be illustrated with a few model calculations in a four-terminal geometry as depicted in Fig. 7.4. The quantity under
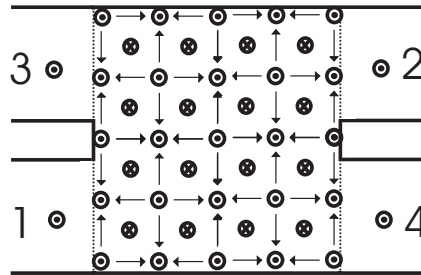

Figure 7.4: Four-terminal setup for calculating the Hall resistance R_H. A magnetization texture is fitted in the central device, while in the leads, the magnetization is pointing out of the plane of the paper.
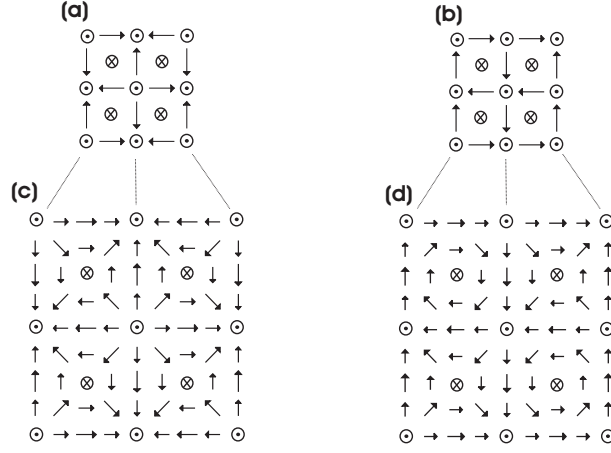
Figure 7.5: Basic unit cells for the magnetization texture used in the numerical calculations. The magnetization direction at every site is indicated by an arrow. Magnetization is projected onto the plane of the paper: a longer arrow stands for a longer projection. The textures in (a,c) have a nonzero net chirality and give therefore rise to a topological Hall effect. The textures in (b,d) only differ slightly from (a,c), but they have a zero net chirality and give no topological Hall effect at all. The larger unit cells (c,d) are obtained by scaling up the smaller ones.

consideration is the Hall resistance R_H as it was defined in the preceding chapter [see the discussion around Eq. (6.11)]: $R_H = 1/2\,(R_{12,34} - R_{34,12})$. To stress the importance of topology in the observed Hall effect, results will be shown for two magnetization textures that are at first sight similarly looking, but which will give completely different results. Some details about these magnetization textures will now be given first.

We start from the magnetization textures shown in Figs. 7.5(a)/(b). The magnetization has constant magnitude, but changes its direction according to the arrows drawn on every lattice site. In Fig. 7.5(a), the solid angle subtended by the magnetization directions is equal to $\Omega = +\pi$ for every single lattice cell, while in Fig. 7.5(b) it is $\Omega = +\pi$ for one half of the lattice cells and $\Omega = -\pi$ for the other half [the sign of the solid angle depends on the rotation direction of the field: it is positive (negative) for a counterclockwise (clockwise) rotation]. Translating this into the flux model, we would have corresponding fluxes of $\Phi/\Phi_0 = \pm 1/4$ through single lattice cells. In Fig. 7.5(a), all fluxes have the same sign and would add up to a net total flux of $4\Phi_0$ through the complete magnetization texture. On the other hand, the opposite fluxes in Fig. 7.5(b) would cancel each other exactly and give a net flux of zero. One says that the structure of Fig. 7.5(a) has a nonzero chirality, while in Fig. 7.5(b) the chirality is zero. In the first case, one would expect a net Hall effect, while the second one gives no Hall effect at all. By this simple reasoning, it is clear that the topology of the magnetization texture is of prime importance.

We can scale up the magnetization textures of Figs. 7.5(a)/(b) by introducing extra lattice sites in between the original sites, and by interpolating the direction of the magnetization at these new sites between those of the original ones. For example, scaling up the magnetization textures in Figs. 7.5(a)/(b) once, one finds the textures depicted in Figs. 7.5(c)/(d). Since the magnetization now varies more slowly from site to site, the solid angle subtended by a single cell of the lattice, and thus the corresponding effective flux piercing through, is smaller. The upscaling procedure can be repeated a number of times: every time we scale up the cell, it will comprise four times the original number of sites, so that the average flux per lattice cell will be decreased by a factor of four. It should be noted that although the effective flux per lattice cell for the original magnetization texture is homogeneously distributed (exactly $\Phi_0/4$ per lattice cell), this is not longer the case for the textures found by scaling up the first one.

The calculations in this section will be done with a 16×16 cell found by scaling up the magnetic textures in Figs. 7.5(a)/(b) two times. We will consider a square geometry as in Fig. 7.4 consisting of 65×65 sites, in which 16 such magnetization cells are fitted. The four attached leads have a width of 30 sites, and the magnetic field in these leads is completely fixed, pointing out of the plane of the paper. Results for the Hall resistance R_H as a function of the energy above the bottom of the spin-up subband are shown in Fig. 7.6. The exchange splitting was chosen to be $\Delta = 2gM = 100t$ in order to make sure we are in the adiabatic regime (see also next section). When the magnetization cell with nonzero chirality [derived from Fig. 7.5(a)] is used, a nonzero R_H is clearly observed in Fig. 7.6. In fact, one can clearly see the integer quantum Hall effect with its well-defined plateaus at $R_H = h/(e^2 n)$ for integer n [33]. This regime could be expected: mapping the
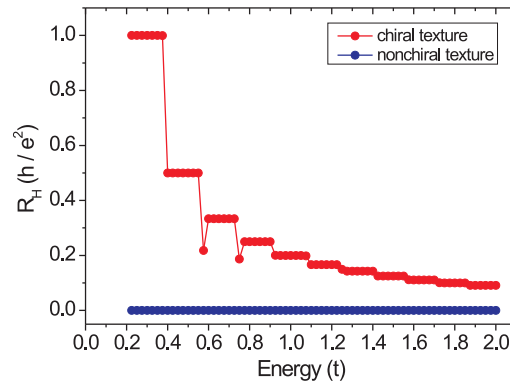

Figure 7.6: Hall resistance as a function of energy above the bottom of the spin-up subband. Only the chiral magnetization texture gives a nonzero Hall effect.

82

magnetization texture onto flux tubes would give an average flux of $\Phi/\Phi_0 = 1/64$ per lattice cell, leading to a cyclotron radius $r_C = 10a$ (for $E_F = t$) which is smaller than the system size. On the other hand, for the magnetization distribution derived from Fig. 7.5(b), no Hall effect is observed in Fig. 7.6 as expected.

When we did the mapping onto the flux model, we found perfect overlapping with the magnetization model results presented in Fig. 7.6. It can be claimed that this perfect overlap does not come as a surprise because in the quantum Hall regime the Hall resistance is quantized into exact plateaus. However, by using magnetization textures that are scaled up more than two times one can reduce the effective magnetic fluxes to values outside the quantum Hall regime. Even in such calculations, the overlap between the magnetization and the flux model was found to be always exact within our numerical accuracy. Nevertheless, the main point is that a Hall effect can be observed that is due to the electron adiabatically following a certain magnetization structure, and which does not invoke any real magnetic flux nor any form of spin-orbit coupling. This point is clearly demonstrated by the results in Fig. 7.6.

7.4 Transition between nonadiabatic and adiabatic regime

7.4.1 Adiabaticity criteria

For the topological Hall effect to appear, the electron spin should follow adiabatically the local magnetization direction. It is intuitively clear that this happens when the exchange splitting is large enough, in which case spin-flip transitions are energetically unfavorable. In this section, we will quantify what is meant with "large enough".

For an electron placed at rest in a time dependent magnetic field, as in Sec. 7.2.2, the adiabaticity criterion yields $\omega_s/\omega \gg 1$, with ω_s the spin precession frequency and ω the rotation frequency of the magnetic field. For the topological Hall effect, it is the electron that moves through a spatially varying magnetic structure, so the rotation frequency ω should be replaced by the inverse of a time scale τ that quantifies how fast the electron "sees" the magnetization change upon its movement through the structure. When no disorder is present in the system, it is clear that this time scale τ is given by $\tau = \xi/v_F$, with v_F the Fermi velocity of the electron, and ξ a characteristic distance over which the magnetization changes its direction substantially (e.g., by an angle π). The adiabaticity criterion in the ballistic regime thus yields

$$Q = \frac{\omega_s \xi}{v_F} \gg 1. \tag{7.24}$$

When introducing disorder in the system, it is clear that this criterion is still valid as long as the mean free path l_m is larger than ξ. However, when going to the strongly diffusive regime $l_m < \xi$, two different time scales τ appear in the literature and there is still a discussion going on about the relevant one [109–113]. Intuitively, one might expect that the relevant time scale would now be the time the

electron needs to diffuse over a distance ξ, i.e., the Thouless time $\tau_{\text{th}} = (\xi/l_m)^2 \, \tau_m$. This was put forward by Loss and coworkers [109, 110], and leads to the criterion

$$Q \gg \frac{l_m}{\xi}. \qquad (7.25)$$

Since $l_m/\xi < 1$ in the diffusive regime, this criterion tells us that adiabaticity is reached faster in a strongly disordered system compared to the ballistic one, and it is therefore referred to as the "optimistic criterion" in the literature. On the other hand, analytical calculations by Stern [111] have found that the relevant time scale is the elastic scattering time $\tau = \tau_m$, leading to a more pessimistic criterion

$$Q \gg \frac{\xi}{l_m}. \qquad (7.26)$$

These criteria were derived while studying Berry phase interference effects in (ring) structures that are subjected to a spatially varying magnetic field. The pessimistic criterion predicts the need for experimentally unrealizable large magnetic fields to observe such effects, while the optimistic criterion would allow for such an experiment given a sufficiently disordered system. Unfortunately, in a paper of van Langen *et al.* the pessimistic criterion was confirmed by a semiclassical analysis [112], and later numerically by Popp *et al.* [113]. In subsequent sections, we will have a closer look at the transition point between the adiabatic and nonadiabatic regimes for our problem of the topological Hall effect, and try to shed some more light on the discussion.

7.4.2 Calculation of the Hall resistivity

To resolve the issue of finding the correct adiabaticity criterion in the diffusive regime, one could think of calculating the Hall resistance R_H as a function of the adiabaticity parameter Q and compare the rate at which the adiabatic regime is reached for samples with different mean free paths. However, the Landauer-Büttiker formalism we use for calculating R_H describes a phase coherent (mesoscopic) system, and all properties of such system are heavily dependent upon the exact placement of impurities throughout the system. This means that the Hall resistance R_H will be different for different disorder configurations, even when they are characterized by the same mean free path. Although such resistance fluctuations are an integral part of the physics of mesoscopic systems [6], they make a quantitative comparison of R_H between samples with different mean free paths useless: the results will depend on the particular choice of disorder configuration in every sample.

We would like to compare properties of a macroscopic system, i.e., a system with a finite phase coherence length in which such fluctuations are absent. For doing so, one can introduce some kind of (phase) averaging over different disorder configurations to find a description of the transport properties in terms of a macroscopic material constant, like the Hall resistivity. Some care should be taken in

defining such an averaging procedure: e.g., just calculating the mathematical average $R_H = \frac{1}{N} \sum_{i=1}^{N} R_H^i$ of the Hall resistances R_H^i found for N different impurity configurations does not give a quantity that is directly related to the Hall resistivity ρ_H of a macroscopic system. We have developed an averaging procedure based on the idea that a macroscopic system ($L \gg L_\phi$) can be thought to consist of smaller phase coherent sections of size $L \approx L_\phi$. For every smaller section, we can use the Landauer-Büttiker formalism to derive its transport properties, and the properties of a macroscopic system can then be found by attaching such sections in an incoherent way. Since a more detailed discussion on our particular averaging procedure and the corresponding Hall resistivity ρ_H is rather technical, it is given in Appendix G at the end of this thesis.

7.4.3 Results

In this section, plots for the Hall resistivity ρ_H will be shown as a function of the adiabaticity parameter $Q = \omega_s \xi / v_F$ for different values of the mean free path: Q can be changed by tuning the exchange splitting Δ, since $\hbar\omega_s = \Delta$. This will allow us to determine whether the adiabatic regime is reached faster or slower as the mean free path is decreased, and thus whether the optimistic [Eq. (7.26)] respectively the pessimistic criterion [Eq. (7.25)] is the correct one.

The starting point for obtaining ρ_H with the procedure described in Appendix G is the structure that was shown in Fig. 7.4: a square region of 65×65 sites is connected to leads with a width of 30 sites. The magnetization texture in the square region is now obtained by scaling up the unit cell in Fig. 7.5(a) three times, giving us a magnetization structure of 64×64 sites. For this particular texture, the shortest distance over which the magnetization rotates by an angle π is $\xi \approx 22$ sites. The magnetization now varies slowly enough so that the effective magnetic flux the electrons see when hopping through the lattice lies far outside the quantum Hall regime. In the leads, the magnetization is chosen to be perpendicular to the plane of the leads (pointing out of the plane of the paper), and is kept constant throughout.

For a given mean free path, 500 different impurity configurations are then generated. Subsequently, 4900 structures as in Fig. 7.4, with impurity configurations chosen randomly from these 500, are wired together in a 70×70 array using the wiring scheme in Fig. G.2 of Appendix G, and the Hall resistivity ρ_H is calculated with the averaging procedure described there. It was made sure that the calculated value of ρ_H converged in the sense that it does not change by either choosing more than 500 impurity configurations, nor by attaching more than 4900 sections.

Results for the quasiballistic regime $l_m > \xi$ are shown in Fig. 7.7. For both mean free paths $l_m = 64a$ and $l_m = 32a$ the adiabatic limit is reached simultaneously for a value of $Q \approx 20$: from this point on, the resistivity stays constant upon increasing Q further. This is in good agreement with the criterion $Q \gg 1$ expected in this regime of parameters [Eq. (7.24)]. It can further be seen that the adiabatic value of $\rho_H \approx 5 \times 10^{-3} \hbar/e^2$ is practically independent of the mean free path. We furthermore checked numerically that this value is the same as the one that would
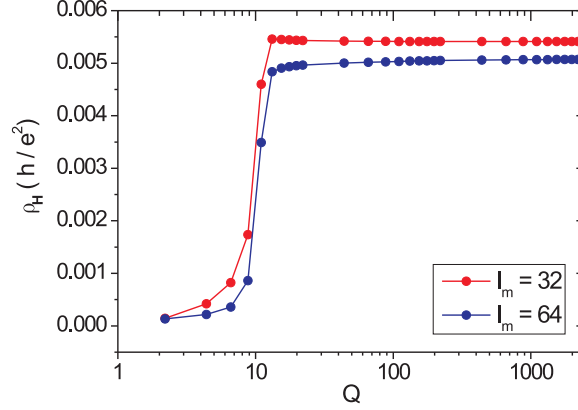
Figure 7.7: Hall resistivity as a function of the adiabaticity parameter Q for mean free path values $l_m > \xi$. The adiabatic limit is reached when $Q \gg 1$.

be obtained by mapping the magnetization model to the effective magnetic flux model (defined in Sec. 7.3.1).

In the nonadiabatic limit, the Hall resistivity does not increase smoothly with increasing the exchange splitting. Rather, ρ_H stays almost zero for small Q and an abrupt transition takes place around $Q \approx 20$ which corresponds to the exchange splitting Δ equaling the Fermi energy ($E_F = 1t$ above the bottom of the spin-up subband in our calculations). So the adiabatic limit is reached on a short scale as soon as the spin-down subband lies above the Fermi energy.

The diffusive regime ($l_m < \xi$) is studied in Fig. 7.8(a). Generally speaking, the same behavior as before can be observed: an abrupt transition takes place around $Q \approx 20$ after which the Hall resistivity takes again the same value of $\rho_H \approx 5 \times 10^{-3} \hbar/e^2$ independent of the mean free path. However, looking closer at the transition point, one can clearly see that the adiabatic limit is reached more slowly for the mean free path $l_m = 9a$: ρ_H first overshoots its adiabatic value, and then slowly converges to it. This difference is made clear in Fig. 7.8(b), where we plotted the difference between the Hall resistivity ρ_H and the adiabatic value it reaches (so that all curves converge to 0), for mean free paths $l_m = 9a, 12a,$ and $16a$. In this figure, there is a clear tendency of slower convergence upon decreasing the mean free path. This speaks in favor of the pessimistic adiabaticity criterion. Although for our limited range of parameters the two adiabaticity criteria do not differ very much quantitatively, namely $Q \gg 0.45$ versus $Q \gg 2$ for $l_m = 9a$, the optimistic criterion would predict the opposite behavior.
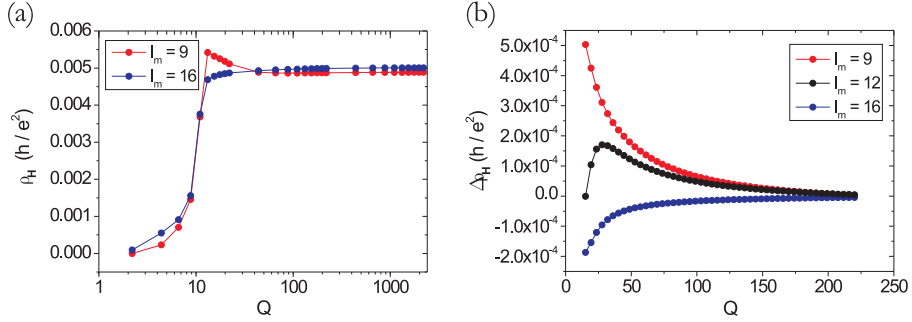
Figure 7.8: Hall resistivity as a function of the adiabaticity parameter Q for values of the mean free path in the diffusive regime. In (b) the region $20 < Q < 250$ is zoomed in upon. The curves in this plot are shifted so they all converge to zero: $\Delta\rho_H(Q) = \rho_H(Q) - \rho_H(Q \to \infty)$.

7.5 Conclusions

In this chapter, we have shown numerical calculations confirming the existence of a fully topological Hall effect, that is due to the Berry phase an electron picks up when moving adiabatically in a noncoplanar magnetization texture. In the adiabatic regime, the governing Hamiltonian can be mapped onto a model of spinless electrons moving in a magnetic flux. Both models indeed give the same numerical results for the Hall resistance/resistivity. A closer look at the transition point between the nonadiabatic and adiabatic regime revealed a rather abrupt transition upon increasing the exchange splitting. The transition takes place around the point where the spin-down subband becomes depopulated. Furthermore, we were able to find confirmation for the pessimistic adiabaticity criterion in Ref. [111] by looking at the transition point for different mean free paths in the strongly diffusive regime. In this regime, a special method for phase averaging was introduced for getting rid of conductance fluctuations, which enabled us to describe the transport properties of a large system ($L > L_\phi$) in terms of a Hall resistivity.